



Article

Femtosecond Laser-Processed, Copper-Coated Stainless Steel Implants Promoting In Situ Calcium Phosphate Crystallization for Orthopedic Application

Albena Daskalova ^{1,*}, Maja Dutour Sikirić ², Liliya Angelova ^{1,*}, Tihomir Car ², Ana-Marija Milisav ², Stuart Neil ³ and Abeer Shaalan ⁴

- ¹ Institute of Electronics, Bulgarian Academy of Sciences, 1784 Sofia, Bulgaria
- ² Ruđer Bošković Institute, 10000 Zagreb, Croatia; sikiric@irb.hr (M.D.S.); tihomir.car@irb.hr (T.C.); milisav@irb.hr (A.-M.M.)
- Department of Infectious Diseases, Faculty of Life Sciences & Medicine, School of Immunology & Microbial Sciences, King's College London, London WC2R 2LS, UK; stuart.neil@kcl.ac.uk
- ⁴ Center for Oral, Clinical and Translational Sciences, Faculty of Dentistry, Oral & Craniofacial Sciences, King's College London, London SE1 9RT, UK; shaalan.abeer@kcl.ac.uk
- * Correspondence: albdaskalova@gmail.com (A.D.); lily1986@abv.bg or liliya_angelova@ie.bas.bg (L.A.)

Abstract

Today, the engineering of load-bearing bone tissue after severe trauma still relies on metal-based (Ti, CoCrMo alloys or stainless steel) permanent implants. Such artificial scaffolds are typically applied in the body and come into direct contact with the recipient's cells, whose adhesion affects the patient's implant acceptance or rejection. The present study aims to create a nano-rough texture by means of ultra-short femtosecond laser (fs)-induced periodicity in the form of laser induced periodic surface structures (LIPSS) on the surface of a stainless steel implant model, which is additionally functionalized via magnetron-sputtering with a thin Cu layer, thus providing the as-created implants with a stable antimicrobial interface. Calcium phosphate (CaP) crystal growth was additionally applied due to the strong bioactive interface bond that CaPs provide to the bone connective tissue, as well as for the strong interface bond they create between the artificial implant and the surrounding bone tissue, thereby stabilizing the implanted structure within the body. The bioactive properties in the as-created antimicrobial hybrid topographical design, achieved through femtosecond laser-induced nanoscale surface structuring and micro-sized CaP crystal growth, have the potential for subsequent practical applications in bone tissue engineering.

Keywords: ultra-short laser processing; LIPSS; nanostructuring; antiviral properties; hierarchical surface texture

1. Introduction

The reconstruction of load-bearing bone tissue following severe trauma remains a critical challenge in orthopedics. Globally, approximately 178 million new fractures were registered in 2019, with a rising trend driven by aging populations [1]. In Europe, the EU6 countries experienced about 2.7 million fragility traumas in 2017, a figure projected to increase to 3.3 million by 2030 [2,3]. Hip fractures alone accounted for nearly 700,000 cases across Europe between 2014 and 2024 [4]. Permanent metallic-based implants—particularly titanium (Ti) and stainless steel (SS)—continue to be the gold standard, especially in hip reconstructions due to their excellent mechanical strength, toughness, and fatigue resistance. However, the long-term success of such implants depends not only on bulk mechanical



Academic Editor: Abel Moreno

Received: 14 October 2025 Revised: 27 October 2025 Accepted: 4 November 2025 Published: 5 November 2025

Citation: Daskalova, A.; Dutour Sikirić, M.; Angelova, L.; Car, T.; Milisav, A.-M.; Neil, S.; Shaalan, A. Femtosecond Laser-Processed, Copper-Coated Stainless Steel Implants Promoting In Situ Calcium Phosphate Crystallization for Orthopedic Application. *Crystals* 2025, 15, 954. https://doi.org/10.3390/ cryst15110954

Copyright: © 2025 by the authors. Licensee MDPI, Basel, Switzerland. This article is an open access article distributed under the terms and conditions of the Creative Commons Attribution (CC BY) license (https://creativecommons.org/licenses/by/4.0/).

Crystals **2025**, 15, 954 2 of 15

properties, but also on the interface and stable connection between the implant and the host bone. Specifically, cellular adhesion, osseointegration, corrosion resistance, and prevention of infection are key factors in ensuring implant acceptance and stability [5,6].

Surface modifications have emerged as a powerful tool for augmenting the biological performance of such implants. In particular, micro- and nanoscale topographies can influence protein adsorption, cell attachment, and differentiation, while functional nanocoatings can confer bioactivity and suppress microbial colonization [6,7]. Within the range of surface patterning strategies, femtosecond laser-induced periodic surface structures (LIPSS) offer a highly precise way to fabricate nanoscale textures, grooves, and regularly spaced features while keeping heat-affected areas to a minimum. This level of control enables the design of surfaces that discourage bacterial colonization and simultaneously foster the adhesion and differentiation of osteogenic cells [8,9]. The use of femtosecond lasers for surface texturing has emerged as a highly effective strategy to modify the structural and chemical characteristics of metallic surfaces. Due to its ultrafast pulse duration, minimal thermal impact, sub-micrometer precision, and ability to generate self-organized nanostructures, this technique offers exceptional control over surface design [10–12]. In parallel, antimicrobial functionalities may be further enhanced by the surface deposition of elements such as copper (Cu), which is known for its broad-spectrum antimicrobial efficacy combined with favorable cytocompatibility when applied at appropriate doses [7,13].

Another critical component of successful bone implants is the growth of calcium phosphate (CaP) phases—especially hydroxyapatite or related forms—which mimic the mineral component of bone [14,15]. CaP coatings, and specifically in situ CaP crystallization, improve the chemical affinity between the implant surface and bone, promote osteoblast function and mineral deposition, and enhance the mechanical anchorage of bone in contact with the implant [5]. Coatings of CaP can also moderate corrosion or ion release of metallic substrates, thereby enhancing biocompatibility and thus ensuring implant acceptance and osteointegration [6].

The novel hybrid approach combining femtosecond laser-induced nano-texturing (LIPSS of stainless steel), copper deposition via magnetron sputtering, and subsequent optimization of CaP crystal growth promises to address multiple challenges simultaneously: (i) mechanical and structural stability from stainless steel, (ii) antimicrobial and even antiviral (as our group demonstrates in the current study) interface via combined action of LIPSS and Cu, (iii) favorable nano-topography to control bacterial adhesion and cell response, and (iv) robust CaP growth for osseointegration and interface bonding [7–9,13]. Such a design strategy may lead to implants with a reduced risk of infection and improved integration into host tissue. Lutey et al. [16], for example, demonstrated that femtosecond LIPSS on 316L stainless steel significantly reduce bacterial retention, highlighting the crucial role of nanoscale morphology in modulating microbial adhesion rather than surface wettability alone. In parallel, Wu and colleagues comprehensively reviewed copperdoped titanium-based implants, reporting that controlled copper incorporation not only imparts strong antibacterial properties but also supports osteogenic differentiation and reduces peri-implant bone resorption in vivo [17]. Complementary studies performed by Wojcieszak et al. [18] further showed that magnetron-sputtered Cu-containing thin films exhibit composition-dependent antibacterial activity against both S. aureus and E. coli, while maintaining good cytocompatibility when copper content/concentration is optimized. Moreover, Oyane et al. [19] demonstrated that laser-assisted surface activation promotes calcium phosphate nucleation and coating adhesion, enabling the formation of bioactive layers that enhance osseointegration. Collectively, these studies support the concept that combining femtosecond laser nano-texturing, copper functionalization, and optimized

Crystals **2025**, 15, 954 3 of 15

CaP deposition could yield multifunctional implant surfaces with improved antimicrobial resistance, structural stability, and biological integration.

In this work, we present a newly developed method for the design of stainless steel bone implant surfaces by means of fs-laser-induced nano-rough LIPSS, coated with Cunano thin films, which tightly replicate the nano-topography of the created LIPSS and calcium phosphate in situ micro-crystallization. The generated novel hierarchical structures were characterized by scanning electron microscopy (SEM), energy-dispersive X-ray spectroscopy (EDX), micro-Raman spectroscopy, and 3D profilometry. As a preliminary biological evaluation, antiviral properties were also studied. We experimentally investigated how the combination of topography, chemistry, and bioactivity can be tuned to produce a multifunctional novel implant surface ideally suited for orthopedic applications.

2. Materials and Methods

2.1. Stainless Steel Samples

Cold-rolled, mirror-polished, bright annealed (BA)-finished stainless steel (SS) samples (AISI 304–304L/DIN standard 1.4301-1.4307—Cr 18–20%, Ni 8–10.5%) with dimensions of 1×1 cm and a thickness of 1 mm were used as primary material (ARST OOD, Stara Zagora, Bulgaria) [20]. Before and after femtosecond laser treatment was performed, the plates were incubated for 10 min in 70% ethanol in an ultrasonic bath (UST1-100t, Siel Ltd., Varna, Bulgaria), cleaned with ddH₂O, and dried in air.

2.2. Femtosecond Laser Processing and Cu Magnetron Post-Modification of the Stainless Steel

Femtosecond laser surface texturing was performed by means of a Ti:Sapphire laser system (Solstice ACE, MKS Spectra-Physics, Milpitas, CA, USA), operating at an output power of P = 6 W, a central wavelength of λ = 800 nm, pulse duration of τ = 70 fs, and a repetition rate of v = 1 kHz. The system is coupled to an XYZ motorized translation stage (Thorlabs, Newton, NJ, USA), controlled via Kinesis v1.14.45 software (Thorlabs, Newton, NJ, USA). The Gaussian beam profile is focused to a spot size of 24.61 µm (measured at 1/e² of the maximum intensity) through a 10 cm focusing lens. Mirror-polished stainless steel (SS) substrates were irradiated following a scanning strategy based on the generation of parallel lines separated by $dx = 50 \mu m$. Surface processing was achieved via precise femtosecond laser ablation conducted in ambient air, employing raster scanning of the perpendicularly oriented SS plates in the X–Y direction so groove arrays with controlled geometrical features, structural morphology, and transverse profile are fabricated. By precise control of the distance in X direction via Kinesis software v1.14.45 (dx was fixed at 50 µII), arrays of parallel grooves between Y laser scanning direction were achieved. Two distinct texturing regimes were implemented to induce nanometric laser-induced periodic surface structures (LIPSS), a class of self-organized features that enhance surface functionality at the nanoscale. Previously optimized laser parameters (power and scanning velocity) were applied as follows: (1) P = 40 mW, V = 3.44 mm/s and (2) P = 20 mW, V = 3.44 mm/s. Comprehensive analyses of the chemical composition, morphological evolution, and wetting behavior of the laser-structured surfaces are presented in detail elsewhere [21]. To further tailor the surface properties, a subsequent magnetron sputtering step was employed for copper (Cu) thin layer deposition.

Following laser texturing, copper thin films were deposited by DC magnetron sputtering (CMS-18, K. J. Lesker, Clairton, PA, USA) using a 99.99% Cu target. Argon was supplied at 13–14 sccm (working pressure p (Ar) ≈ 0.67 p) and target power was 100 W. The target-to-substrate distance was 17 cm at a cathode inclination of 14.5°. The deposition rate, calibrated by a quartz-crystal microbalance and verified by step-profilometry on Si, was 0.18 nm/s. All samples (polished control and LIPSS-textured) received identical sputtering

Crystals **2025**, 15, 954 4 of 15

runs to ensure comparable Cu coverage; no intentional substrate heating or substrate bias was applied. To avoid cytotoxicity while preserving antibacterial properties, the Cu content was optimized in a series of experiments, and the final Cu nominal film thickness was determined to be \sim 200 nm.

2.3. In Situ CaP Crystalization

As the last step of SS surface functionalization, CaP coatings were prepared in situ. A two-step procedure was applied to deposit CaP [22,23]. In the first step, amorphous calcium phosphate (ACP) was adsorbed on the surface from freshly prepared suspension by mixing equal volumes of equimolar (c = 20 mM) CaCl₂ and Na₂HPO₄. The pH of Na₂HPO₄ was adjusted to 7.4 with HCl. In the second step, in order to enable ACP transformation into the crystalline phase, the samples were immersed in metastable calcifying solution (MCS) prepared by rapidly mixing equal volumes of CaCl₂ (c = 5.6 mM) and Na₂HPO₄ (c = 4.0 mM, pH = 7.4) solutions. The reactant concentrations in MCS were chosen so that no visible precipitation was detected even after 14 days.

After triple surface functionalization of the samples was performed, three different groups of novel hybrid SS-based implant specimens were formed, as follows: **1.** Cu-0-CaP: control SS, sputtered with Cu + in situ grown CaP crystals; **2.** Cu-1-CaP: fs-nanostructured SS, at P = 20 mW, V = 3.44 mm/s, sputtered with Cu + in situ-grown CaP crystals on top; **3.** Cu-2-CaP: fs-nanostructured SS, at P = 40 mW, V = 3.44 mm/s, sputtered with Cu + in situ-grown CaP crystals on top.

2.4. Surface Characterization: Morphological and Elemental Analysis

The morphology of the surface-functionalized stainless steel bone implant specimens was examined by field-emission SEM Hitachi SU5000, equipped with LYRA I XMU EDS/WDS systems (Hitachi, Tokyo, Japan). Secondary electron micrographs were acquired at $1000\times$ and $5000\times$ magnifications under an accelerating voltage of 20 kV. A deposition of additional conductive carbon coating (thickness of 10 nm) was performed before imaging. The elemental composition of the modified surfaces was further analyzed by energy-dispersive X-ray spectroscopy (EDX) at $10~\rm kV$ and $5000\times$ magnification.

Surface topography and roughness parameters (Rpm—line roughness and Sa- surface area roughness) were characterized using a three-dimensional optical profilometer Zeta-20 (Zeta Instruments, KLA, Milpitas, CA, USA) at 20× magnification. The resulting 3D surface maps represent the average of five independent measurements and were generated and analyzed using the ProfilmOnline software platform (https://www.profilmonline.com, accessed 5 March 2025). The mean size of the CaP crystals was also measured and averaged over 5 different samples from each type.

To assess structural and compositional changes associated with the laser treatment, micro-Raman spectroscopy was performed using a LabRAM HR Visible spectrometer (Horiba, Kyoto, Japan) equipped with a 633 nm He–Ne excitation laser and coupled to an optical microscope BX41 (Olympus, Tokyo, Japan): exposure time—10 s; magnification— 50×10^{-2} .

2.5. Antiviral Studies

The antiviral performance of laser-textured stainless steel (SS) surfaces, both before and after CaP crystallization and copper deposition via magnetron sputtering, was assessed according to the ISO 21702 standard protocol [24], which specifies procedures for measuring antiviral activity on plastics and other non-porous surfaces. The replication-competent, bioluminescent influenza reporter virus (NanoLuc IAV) was used as a model viral pathogen, and untreated SS served as the control substrate. For the antiviral assays, Madin–Darby bovine kidney (MDBK) host cells were seeded into 96-well culture plates at a density of 3.5×10^4 cells per well in 100 μ L of complete Dulbecco's Modified Eagle Medium

Crystals **2025**, 15, 954 5 of 15

(DMEM) supplemented with 10% fetal calf serum (FCS), 1% L-glutamine (200 mM), and 1% penicillin/streptomycin. The plates were incubated for 24 h at 37 °C under a 5% CO₂ atmosphere to allow cell attachment and growth. Subsequently, 100 µL of the IAV viral inoculum $(3.5 \times 10^7 \text{ PFU/mL})$ as determined by plaque assay) was applied to UV-sterilized SS samples and incubated for 1 h at 25 °C in a humidified environment. Following incubation, the inoculum was recovered with 900 µL of complete DMEM then diluted 10 fold (till 10^{-3}). MDBKs were washed with PBS which was aspirated and 30 μ L of GibcoTM Opti-MEMTM reduced serum medium was added per well. Then, 20 μL of recovered and serially diluted inoculum was added to each well and the plate was incubated for 1 h at 37 °C under a 5% CO₂ atmosphere. After 1 h, supernatants were removed and unbound viruses were washed off with PBS. MDBK cells were incubated overnight in Opti-MEMTM at 37 °C in a 5% CO₂ atmosphere to allow viral replication. After 24 h, the antiviral activity was quantified using the Nano-Glo® luciferase assay system and luminescence was measured using a luminometer. To enable quantification of infectious virus recovery from test surfaces in terms of infectious units per milliliter (IU/mL), a standard curve was generated. An independent 96-well plate of MDBK cells was prepared and infected with 10-fold serial dilutions of a virus stock with a known titer determined by plaque assay. After 24 h incubation under identical conditions, NanoLuc activity was measured using the Nano-Glo® luciferase assay system. The resulting luminescence values (in relative light units, RLU) were plotted against the known input virus concentrations ($log_{10} IU/mL$). A linear regression was performed to establish the correlation between log₁₀ (RLU) and \log_{10} (IU/mL), yielding a standard curve with a correlation coefficient (R^2) > 0.98. This curve was subsequently used to convert RLU values from test samples into IU/mL, thereby enabling direct comparison of antiviral efficacy across different surface treatments.

3. Results

3.1. Morphological and Roughness Evaluation of the Cu-CaP Functionalized SS Samples

The surface topography of the novel designed SS-based samples, presented in Figure 1 was obtained by means of SEM micrographs of the cSS (1. Cu-0-CaP) and the two groups of fs-structured Cu-CaP specimens (2. Cu-1-CaP and 3. Cu-2-CaP). A notable feature evident from the images of all three SS groups is the successful nucleation and growth of calcium phosphate crystals within the micrometer range, accompanied by the development of a distinct hierarchical micro/nanostructural architecture across the surfaces. Nevertheless, the quantity, distribution, shape, form, and microporosity of the grown crystals are quite different among samples. While the control samples (1. Cu-0-CaP) show a much smaller amount of unevenly distributed, mainly amorphous, spherical structures, the growth of quite expanded, porous crystal structures is observed on the laser-structured steel samples, which, in the case of Cu-2-CaP group, form a fairly homogeneously distributed crystalline layer on the surface. The observed leaf-like morphology of CaP is characteristic of the apatitic phase, while its formation in the form of spherical aggregates could indicate that the crystals were formed by the transformation of initially deposited ACP [23]. This multiscale structural organization demonstrates the effectiveness of the presented hybrid approach in promoting controlled CaP deposition and complex surface topography formation.

Moreover, as illustrated in the figure (SEM images at higher magnification), the LIPSSs produced via femtosecond laser irradiation remain distinctly visible following the magnetron sputtering process. The periodic nanostructures generated by the laser-induced surface patterning preserve their regularity, spatial arrangement, and orientation after sputtering, irrespective of the two parameter sets employed for stainless steel surface modification (Figure 1—2. Cu-1-CaP and 3. Cu-2-CaP SS samples). In contrast, the control specimen (Figure 1—1. Cu-0-CaP) continues to exhibit a characteristically smooth surface

Crystals **2025**, 15, 954 6 of 15

underneath the Cu thin layer. Furthermore, the characteristic dimensions, orientation, spatial frequency (LSFL with average periodicity of Λ ~770 nm), and overall morphology of the LIPSS formed by the femtosecond laser are consistent with those reported before the Cu-sputtering step, in agreement with previously documented findings by our group [21].

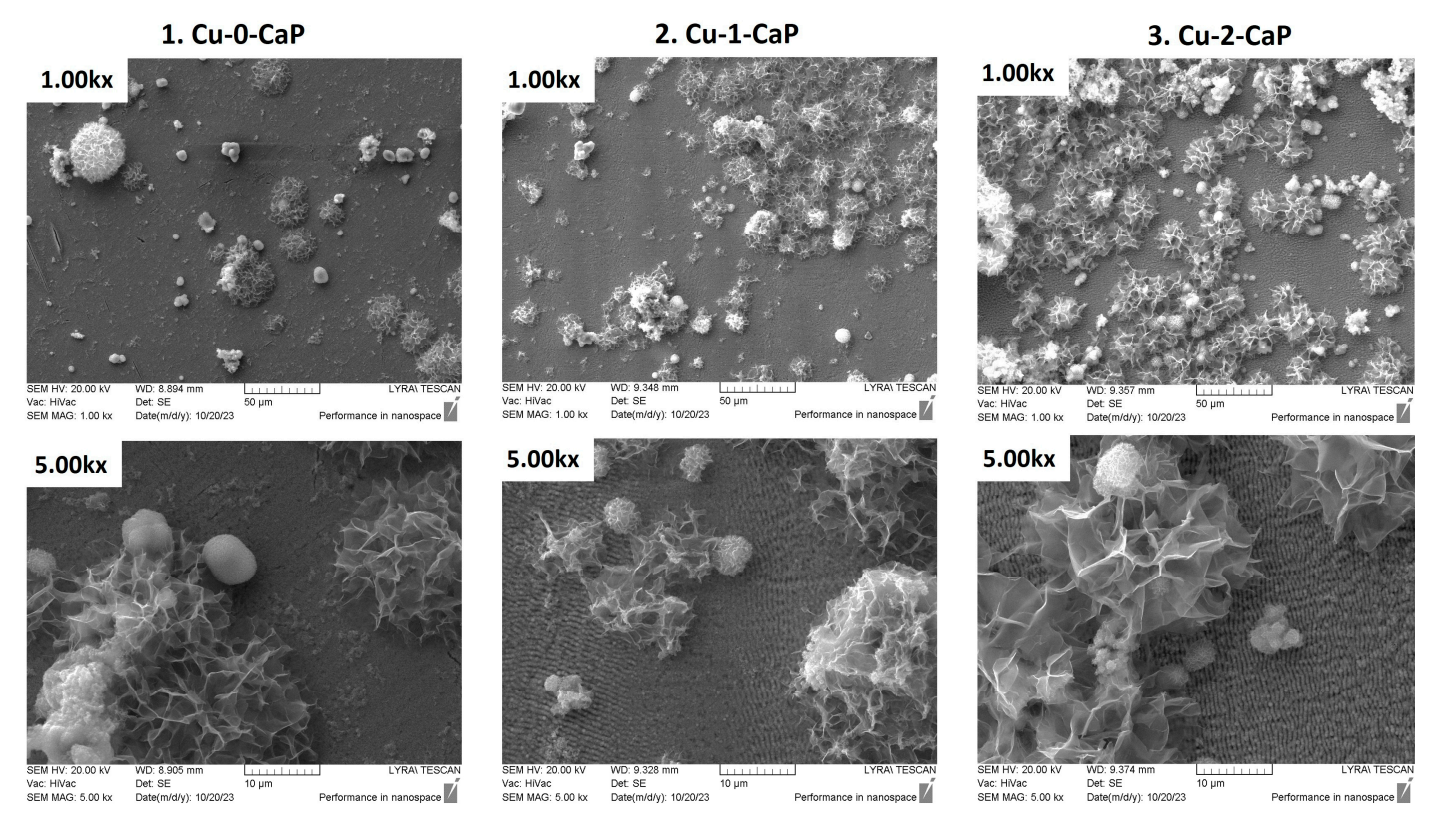


Figure 1. SEM images of: 1. Cu-0-CaP (first column); 2. Cu-1-CaP (second column); and 3. Cu-2-CaP SS samples (third column) taken at $1000 \times$ and $5000 \times$ magnification.

In addition to the microscopic study, roughness testing of the hierarchical SS-based surfaces was also performed. To maximize coverage of the range of micro- and nanostructures created, Figure 2 illustrates representative 2D and 3D surface topography maps of specific zones in the studied samples. The dimensions of the grooves, created by the laser, particularly with respect to depth, width, and transverse profile, are not well defined under the macro CaP crystals formed on top. Nevertheless, the average values of the linear (Rpm) and surface area (Sa) roughness parameters are also provided (Table 1).

Table 1 Averaged values of linear	(Ppm) surface area	roughness (Sa) and	CaP arretale dimensions
Table 1. Averaged values of linear	(Kpiii), Surface area	i rouginiess (5a), and	Car crystais unificisions.

SS Samples	Rpm—Averaged	Sa—Averaged	CaP Crystals Dimensions
1. Cu-0-CaP	1.943 μm	2.211 μm	average height of crystals: 4–6 μm; largest crystal—12.97 μm
2. Cu-1-CaP	1.968 μm	2.201 μm	average height of crystals: 6–9 μm; 19.25 μm (largest crystal)
3. Cu-2-CaP	7.469 μm	6.567 μm	average height of crystals: 8–12 μm; largest crystal—62.43 μm

Crystals **2025**, 15, 954 7 of 15

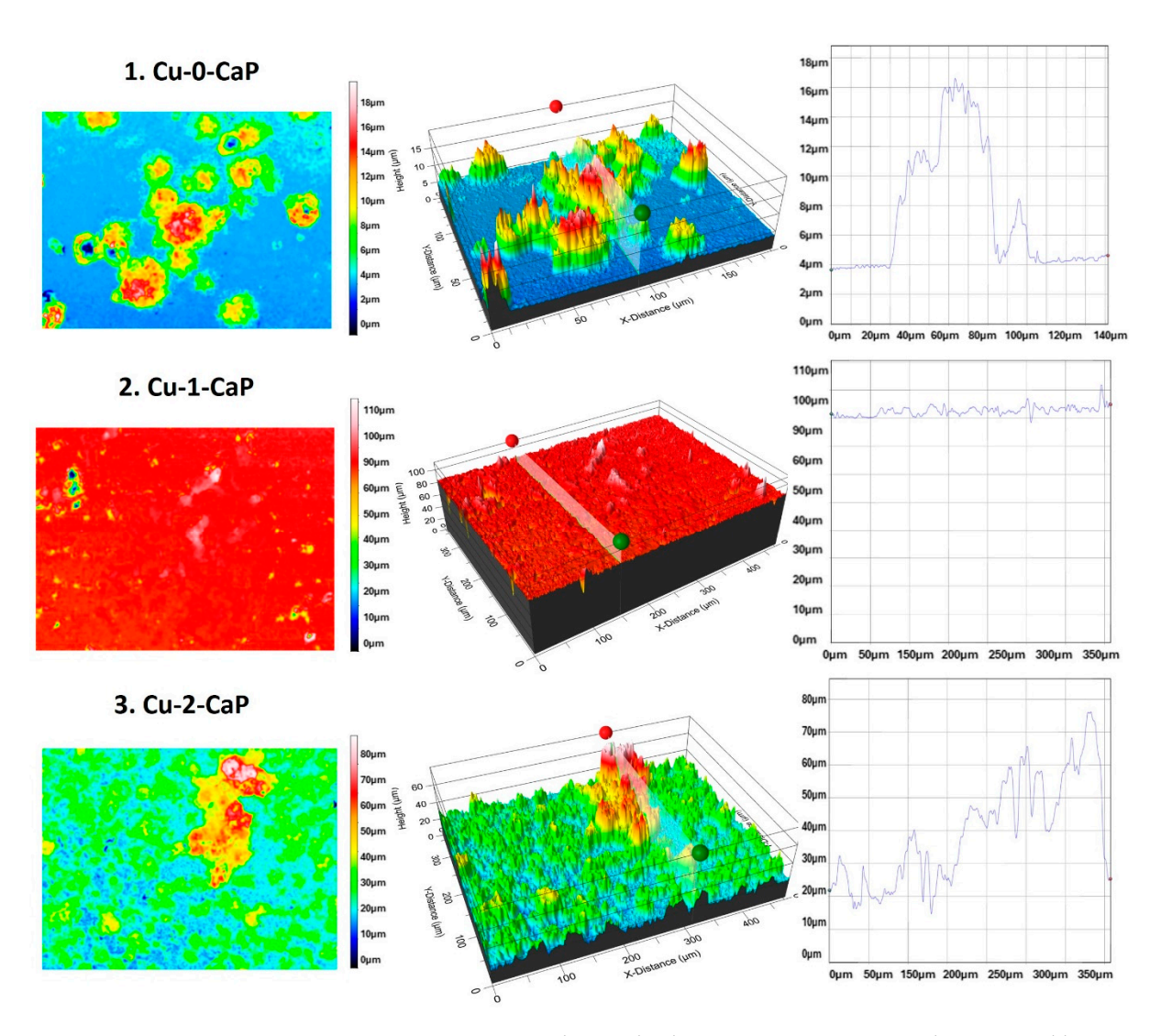


Figure 2. Representative 2D and 3D real-color reconstruction topography maps and linear roughness profiles of: 1. Cu-0-CaP (first line), 2. Cu-1-CaP (second line) and 3. Cu-2-CaP SS samples (third line) taken at 20× magnification.

As can be clearly seen from the images presented, the dimensions of the formed crystals vary in a very broad range, with an average height of crystals of 4–6 μm for 1. Cu-0-CaP to up to a 62.43 μm height for the biggest crystal detected on the surface of 3. Cu-2-CaP SS (average height of crystals: 8–12 μm). The values of the Rpm and Sa parameters of 3. Cu-2-CaP SS samples are about two orders of magnitude larger than those for 1. Cu-0-CaP and 2. Cu-1-CaP, which could be attributed not only to the higher quantity of the crystals, but also to the very porous nature, crystallinity and size of the CaP microstructures deposited on top of the Cu nanolayer and LIPSS beneath it (Figures 1 and 2—3. Cu-2-CaP; Table 1).

3.2. Elemental Characterization of the Cu-CaP Functionalized cSS and fsSS Samples

Simultaneously with the SEM investigations, the elemental composition of the samples was analyzed by energy-dispersive X-ray spectroscopy (EDX) (Figure 3), and a comparative evaluation of copper deposition and CaP crystal growth (at.%) on femtosecond laser–nanostructured stainless-steel surfaces relative to SS samples before in situ crystallization was performed (Table 2). The EDX spectra confirm the presence not only of all the elements characteristic of AISI stainless steel according to DIN 1.4301–1.4307 standards (EN 10088-1:2014) [25], with no extraneous elements detected following laser

surface structuring, but also copper [Cu] deposited by magnetron sputtering and calcium [Ca] and phosphorus [P] were detected and the concentration of the elements (at.%) was established (Figure 3).

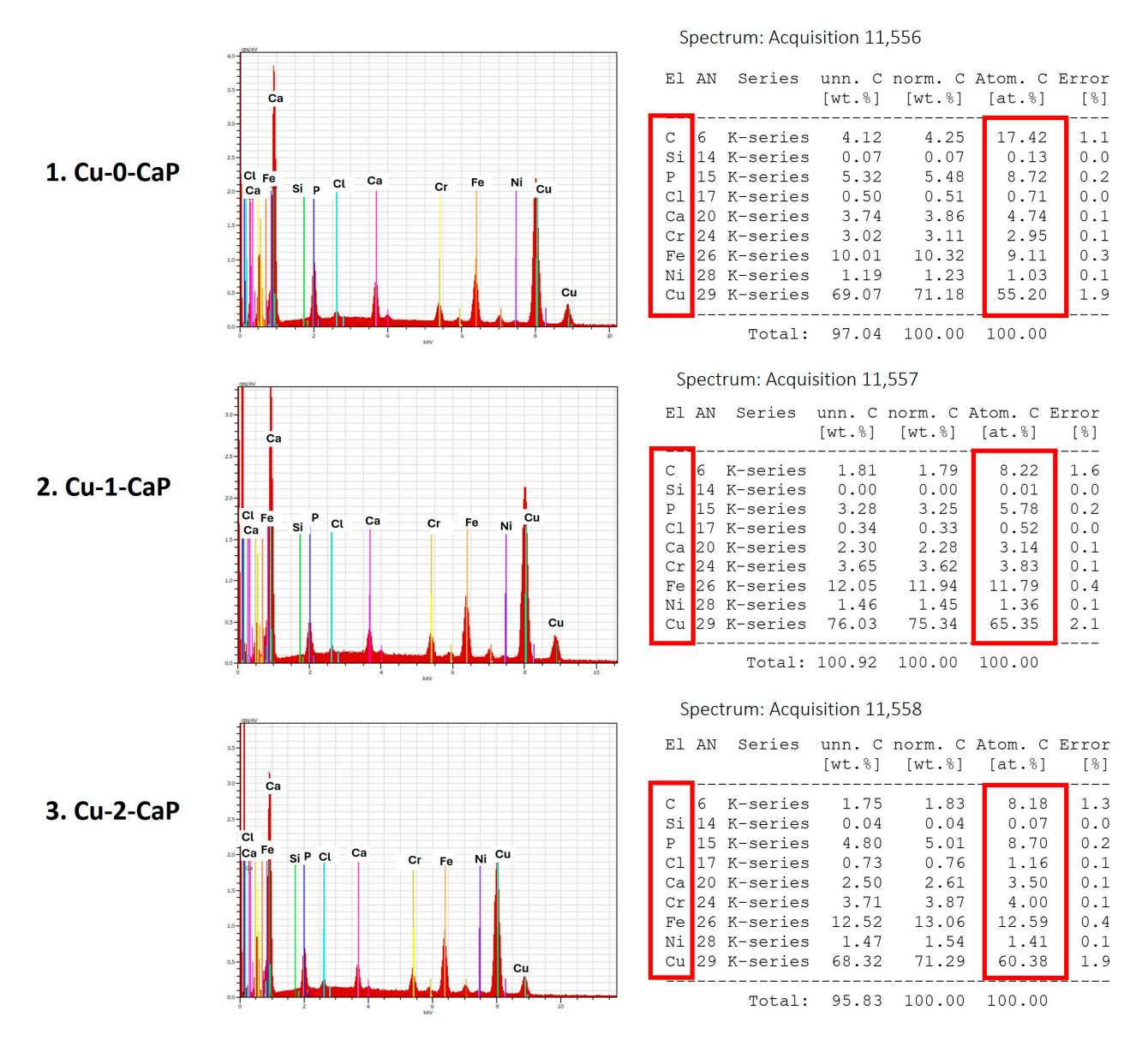


Figure 3. EDX spectra and elemental composition (at.%) of: 1. Cu-0-CaP (first line); 2. Cu-1-CaP (second line); and 3. Cu-2-CaP SS (third line) samples.

Table 2. At.% of Cu, Ca and P of the investigated SS samples.

SS Samples	[at.%] Cu Before CaP Growth	[at.%] Cu After CaP Growth	[at.%] Ca After CaP Growth	[at.%] P After CaP Growth
1. Cu-0-CaP	69.30	55.20	4.74	8.72
2. Cu-1-CaP	76.52	65.35	3.14	5.78
3. Cu-2-CaP	67.59	60.38	3.50	8.70

As summarized in Table 2, the atomic percentage of copper exhibits a slight increase on surfaces patterned with femtosecond LIPSS (2. Cu-1-CaP) compared to the untreated substrates. This enhancement suggests that, under the applied conditions, the nanopatterned topography generated by femtosecond processing promotes more effective Cu deposition, most likely by enhancing the adhesion of Cu to the created nanostructure and

Crystals 2025, 15, 954 9 of 15

thus facilitating improved nucleation sites. The formation of localized modification of the substrate surface creates chemically active regions that promote Cu deposition [26].

In contrast, a reduced Cu atomic percentage was detected across all three stainless steel groups following CaP crystal growth, which is attributed to the deposition of Ca and P and their cumulative contribution to the elemental composition, thereby normalizing the total concentration to 100 at.%.

MicroRaman analysis of magnetron-sputtered SS samples, samples before Cu layer deposition, and the ones on which crystals were subsequently grown, was performed. As illustrated in the Raman spectra in Figure 4, the characteristic Fe₃O₄ peak (magnetite) at 670 cm^{$^{-1}$} [27,28], which appears after laser nanostructuring due to surface oxidation (Figure 4a), remains detectable after Cu sputtering (Figure 4b) and following CaP deposition (Figure 4c). In the Cu-1 and Cu-2 groups, distinct peaks corresponding to CuO at 345 cm^{$^{-1}$} and Cu₂O at 520 cm^{$^{-1}$} are clearly observed [29,30], whereas these peaks are absent in the Cu-0 group (Figure 4b) and the unstructured control SS samples (Figure 4a). A similar trend is noted after CaP deposition on the surfaces, particularly in the Cu-0-CaP group (Figure 4c). The reduced intensity of the Fe₃O₄ and CuO peaks in this case is likely due to the higher CaP content, which partially obscures the characteristic maxima. These observations are consistent with the EDX data (Table 2) as well as SEM and surface roughness analyses.

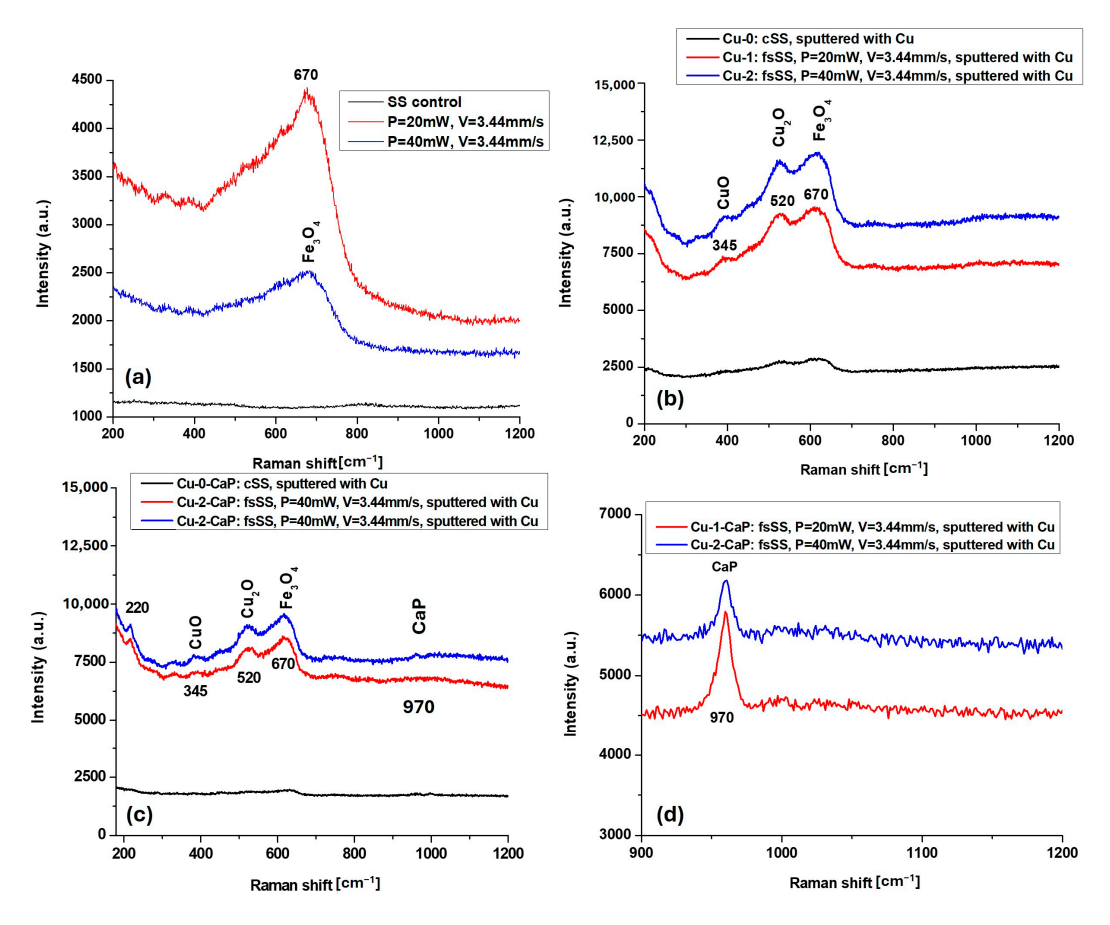


Figure 4. MicroRaman spectra of: (a) cSS, group 1 and group 2 fsSS before, (b) after Cu magnetron sputtering, and (c) after CaP crystal growth; (d) scaled-up zone of the micro-Raman spectrum of (c) in the range of 900–1200 cm⁻¹ at lower intensity (a.u.).

Notably, the Raman signals are more pronounced in the Cu-2 and Cu-2-CaP samples, corresponding to the second set of femtosecond laser parameters used for LIPPS generation on SS surfaces (Figure 4b,c). This enhancement can be attributed to increased surface oxidation induced by femtosecond laser treatment performed at higher power, which

promotes the formation of oxidized species of Fe (Fe₃O₄) and Cu (CuO, Cu₂O). Such features are not observed in control SS samples, whether sputtered or unsputtered (cSS, Cu-0, and Cu-0-CaP), highlighting the influence of laser-induced surface modification on subsequent oxidation and crystal growth.

As can be seen from the scaled-up zone of the micro-Raman spectrum of Cu-1-CaP and Cu-2-CaP samples in the range of 900–1200 cm $^{-1}$, presented in Figure 4d, a peak around 970 cm $^{-1}$, corresponding to the ν_1 symmetric stretching mode of the $PO_4{}^{3-}$ (phosphate) group of the in situ crystallized CaP, is clearly outlined [31]. The shift in the position of this characteristic band of calcium phosphate strongly depends on the phase and structure of the CaP crystals, which in the current case could be attributed mainly to the shift of in the ($PO_4{}^{3-}$) symmetric stretching mode of hydroxyapatite near 960 cm $^{-1}$ to the β -tricalcium phosphate crystalline phase— \sim 970–975 cm $^{-1}$ [32].

3.3. Antiviral Evaluation of Cu-CaP Functionalized Control and fsSS Plates

Cu ions (Cu^+) are released from the surface of the as-coated SS substrate and interact with viral particles, inducing disruption of the viral membrane, thus triggering prevention of viral replication. The release of Cu^+ inactivates viruses upon contact with the surface, which shows a potential for antiviral action [33].

The antiviral performance of copper-functionalized calcium phosphate-coated stainless steel (Cu-CaP) surfaces was evaluated using a NanoLuc IAV reporter system and expressed in infectious units per milliliter (IU/mL) following 24 h infection of MDBK cells. Luminescence data were converted to IU/mL using a previously established standard curve derived from serial dilutions of a known IAV titer. As shown in Figure 5, a dose-dependent decline in viral infectivity was observed across all input inocula; however, the degree of reduction varied significantly among surface treatments and incubation conditions.

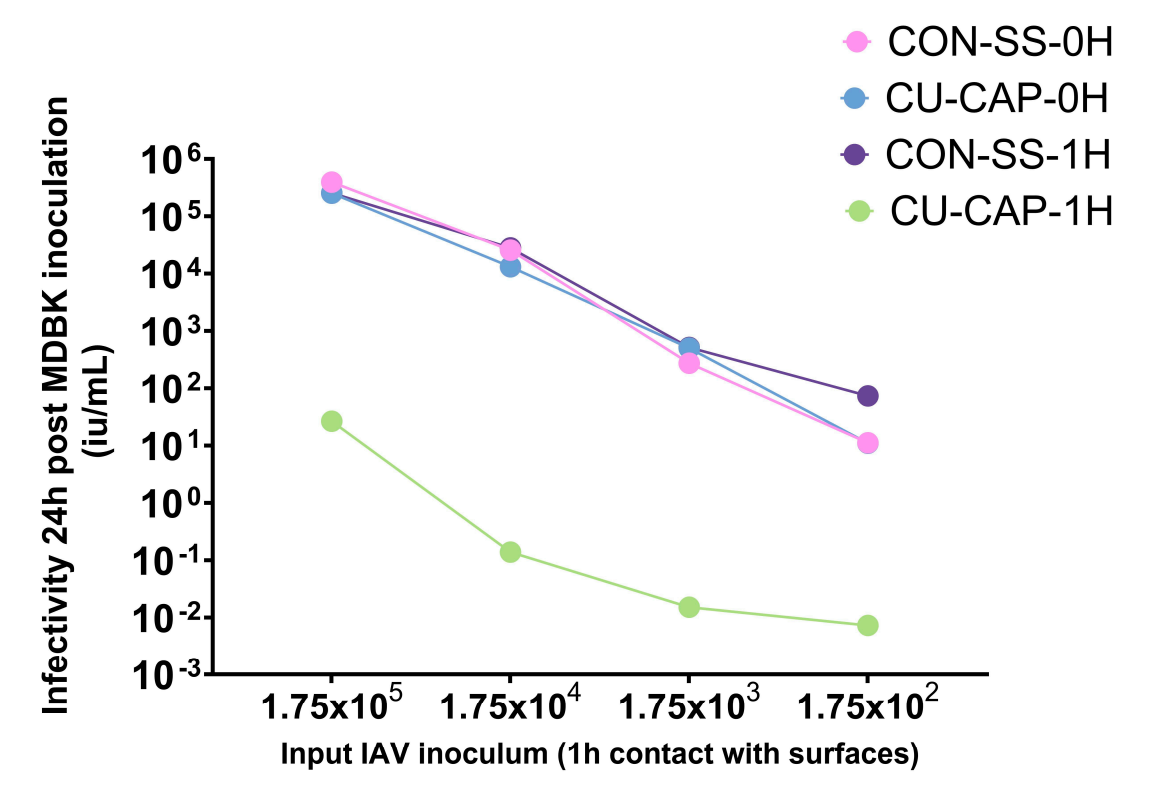


Figure 5. Viral infectivity of MDBK cells measured 24 h post-inoculation using a NanoLuc reporter virus system and expressed in infectious units per milliliter (IU/mL), calculated via a standard curve. Cu-CaP-1H—copper/calcium phosphate-treated stainless steel and CON-SS-1H—untreated stainless steel with 1 h viral exposure. Cu-CaP-0H and CON-SS-0H—back reference controls.

The Cu-CaP-1H group—where the virus was incubated on the treated surface for 1 h—demonstrated a striking reduction in viral infectivity across all inoculum concentrations, with decreases reaching 5–6 log₁₀ IU/mL compared to controls. In contrast, Cu-CaP-0H and CON-SS-0H surfaces, included as baseline (back reference) controls, retained high levels of viral infectivity and showed nearly overlapping curves, indicating minimal inactivation immediately upon surface contact. Similarly, CON-SS-1H, representing unmodified stainless steel after 1 h virus exposure, did not result in significant infectivity loss. These findings highlight the time-dependent antiviral activity of Cu-CaP surfaces, suggesting that extended contact is critical for effective inactivation, likely through cumulative copper ion-mediated disruption and surface-induced viral damage.

4. Discussion

The present study demonstrates that the combination of femtosecond-generated LIPSS, copper functionalization, and calcium phosphate crystallization effectively creates hierarchical surfaces on stainless steel implants with improved bioactivity, structural stability, and antiviral potential. The femtosecond laser texturing technique presented above facilitated the creation of SS surfaces with highly tunable nanoscale architectures. This process simultaneously triggers surface self-organization, leading to the formation of LIPSS with well-defined orientation and periodicity that have been previously proven by our research group to possess antibacterial effect against *S. aureus* and *E. coli.* [21]. The subsequent deposition of copper (Cu) through magnetron sputtering introduces antiviral action to the surface, leading to a synergistic effect of the laser-induced nanostructures and the metallic coating [18], while CaP deposition provides the multifunctional implant surfaces with improved bioactive interface and biological integration [14]. Comprehensive morphological and chemical characterization elucidates how the proposed novel hybrid fabrication approach modulates surface architecture and functional performance, providing a robust framework for designing next-generation orthopedic implant surfaces.

SEM and 3D profilometry analyses revealed that the laser-structured surfaces (Cu-1-CaP and Cu-2-CaP) exhibited significantly enhanced CaP growth compared to unstructured controls (Cu-0-CaP)—Figure 1. CaP crystallization in porous, rough layer-like micrometric structures on the nanopatterned surface was observed. Notably, the Cu-2-CaP group exhibited the highest average crystal heights (8–12 µm) and the largest maximum crystal dimension (~62 μm), suggesting that the specific combination of the laser parameters applied for that treatment (P = 40 mW, V = 3.44 mm/s) produces surface topographies that promote more extensive mineralization. These findings are consistent with previous reports, demonstrating that micro- and nano-scale surface features act as nucleation sites for CaP in situ crystallization, which ultimately improves osteoconductivity and bone-implant interface strength [34]. Oyane et al. [19], for example, demonstrated that laser-assisted biomimetic treatment enhances CaP deposition on polyetheretherketone surfaces by roughening the surface and facilitating heterogeneous calcium phosphate nucleation, resulting in a dense hydroxyapatite layer in simulated body fluid and improved compatibility with osteoblastic MC3T3-E1 cells. Similarly, the higher surface roughness (Rpm \approx 7.5 μ m) observed in the Cu-2-CaP group (Table 1) may enhance the interfacial bonding between host tissue and the stainless steel implant. Jiang et al. [35] achieved comparable roughness values (~7 μm) on titanium surfaces through advanced surface engineering, reporting improvements in both bioactivity and mechanical performance. Likewise, Jahani and Wang [36] highlighted how increased surface roughness (6–7 μm) in Ti13Nb13Zr implants promotes stronger cell attachment and superior mechanical properties.

EDX analysis further confirmed the role of femtosecond surface modification in the degree of Cu functionalization and CaP crystallization. A slight increase in Cu atomic

Crystals 2025, 15, 954 12 of 15

percentage on femtosecond laser–patterned surfaces (Cu-1-CaP) compared to untreated substrates suggests that LIPSS enhance metal adhesion by providing additional high-energy nucleation sites. Following CaP deposition, the incorporation of Ca and P into the total composition, highlights the complementary roles of surface chemistry and topography in controlling the spatial distribution of functional elements on the implant surface—Figure 3, Table 2. The formation of the apatitic CaP phase is important for bone formation, as it supports osteoblast adhesion and proliferation and strengthens the bone–implant interface [27,28]. Rey et al. [37] demonstrated that hydroxyapatite coatings with a Ca/P ratio near 1.67 enhance osteoconductivity and support bone tissue regeneration. Similarly, Kokubo and Takadama [38] emphasized that a phosphate-rich surface biomimetic coating promotes apatite nucleation and growth, further improving the integration of metallic implants with surrounding bone.

The SS nanostructuring also significantly influenced surface chemistry—in the Cu-1 and Cu-2 groups, the presence of oxidized copper species (CuO, Cu₂O) was confirmed by Raman spectroscopy and correlated with previous observations of antibacterial activity [30,31]. This was not the case with Cu-0 and unstructured SS surfaces that did not exhibit such features. These results indicate that combining femtosecond laser treatment with Cu sputtering not only enhances surface oxidation and promotes CaP deposition but may also improve the biological functionality of the surface through controlled Cu oxidation. By replicating the mineral composition of native bone, the hierarchical surfaces fabricated in this study represent a favorable platform for osseointegration, potentially reducing implant failure rates [39]. Micro-Raman analysis provided further insights into the chemical transformations resulting from femtosecond laser processing and Cu deposition. The characteristic Fe₃O₄ peak at 670 cm⁻¹ persisted across all samples, indicating laserinduced oxidation. In the Cu-functionalized groups, pronounced peaks corresponding to CuO (345 cm⁻¹) and Cu₂O (520 cm⁻¹) were detected, while these signals were absent in unstructured stainless steel. After CaP deposition, the intensity of Fe₃O₄ and CuO peaks slightly decreased, likely due to attenuation by the overlaying crystals, which were also detected around 970 cm⁻¹ ($v_1 PO_4^{3-}$), indicating the presence of crystalline β -TCP on the fs structured SS [32]. The enhanced Raman signals in the Cu-2 and Cu-2-CaP samples suggest that with increasing laser power, a rise in surface oxidation was detected, generating additional reactive sites for Cu oxide formation and CaP crystallization. These findings align with prior studies indicating that femtosecond laser-induced oxidation enhances surface bioactivity and antibacterial performance [8,40–42].

The current research demonstrates a tri-modal antiviral effect via physical, chemical, and biofunctional actions. The antiviral activity of the produced specimens is shown in Figure 5. A synergistic effect is monitored from the LIPSS, Cu sputtered, CaP-functionalized stainless steel surface. This arises from the interplay between topographical, chemical, and physicochemical properties of the as-created samples. The laser-induced LIPSSs provide enhanced surface zones and localized electromagnetic hotspots that can trigger oxidative reactions. The Cu magnetron-sputtered thin films additionally promote a controlled release of Cu⁺ ions, which are well known for their antiviral properties that induce disruption of viral envelopes, through oxidative stress [42]. Moreover, a Cu-coated surface layer promotes the formation of reactive oxygen species (ROS), which accelerates further viral disintegration [43]. On the other hand, functionalization with a CaP layer modulates Cu ion release, enhances antiviral efficacy, and simultaneously minimizes cytotoxicity. The combination of these tri-functional approaches provides a surface with improved, sustainable antiviral properties due to physical disruption, ion-mediated oxidation, and biochemical immobilization actions.

Crystals 2025, 15, 954 13 of 15

Further research should be performed to evaluate the in vitro and in vivo behavior of these hybrid surfaces, particularly regarding the cytotoxicity, long-term bone integration, immune response, and antibacterial efficacy under physiological conditions. Additionally, systematic optimization of Cu content, fs laser parameters, and CaP growth could further refine the implant's multifunctionality. Extending this fabrication design strategy to other metallic systems (e.g., titanium alloys) and temporary implant materials (e.g., polymers, composites) could expand its clinical applicability and therapeutic potential.

5. Conclusions

This study demonstrates a novel hierarchical surface design strategy for stainless steel-based implants by integrating femtosecond laser–induced periodic surface structures, magnetron-sputtered copper nano-thin films, and controlled in situ calcium phosphate crystal growth. The combined approach enables precise modulation of surface topography, chemistry, and bioactivity, yielding multifunctional implant interfaces with enhanced biological performance. The work highlights the potential of integrating the presented methods into a versatile platform for designing next-generation orthopedic implants that meet both mechanical and biological demands.

Author Contributions: Conceptualization, A.D. and M.D.S.; methodology, A.D., M.D.S. and L.A.; software, L.A.; validation, A.D., M.D.S. and L.A.; formal analysis, L.A., T.C. and A.-M.M.; investigation, A.D., M.D.S., L.A., A.S. and T.C.; resources, A.D.; data curation, A.D., M.D.S., A.S., S.N. and L.A.; writing—original draft preparation, A.D., M.D.S. and L.A.; writing—review and editing, L.A., A.D. and M.D.S.; visualization, L.A.; supervision, A.D.; project administration, A.D.; funding acquisition, A.D. All authors have read and agreed to the published version of the manuscript.

Funding: This work was supported by the European Union's H2020 research and innovation program under the Marie Sklodowska-Curie grant agreement AIMed no. 861138, 2020–2023; the Bulgarian National Science Fund (NSF) under grant number KP-06-RILA/6 (2024–2026); and the European Union: Horizon Europe program under the Grant Agreement № 101057961, "Surface transfer of pathogens" (STOP).

Data Availability Statement: The original contributions presented in the study are included in the article; further inquiries can be directed to the corresponding authors.

Acknowledgments: The research was carried out with the help of infrastructure purchased under the National Roadmap for Scientific Infrastructure (ELI-ERIC-BG), project D01-351.

Conflicts of Interest: The authors declare no conflicts of interest.

Abbreviations

The following abbreviations are used in this manuscript:

LIPSS laser-induced periodic surface structures

fs femtosecond SS stainless steel

SEM scanning electron microscopy

EDX energy-dispersive X-ray spectroscopy

MDBK Madin–Darby bovine kidney
DMEM Dulbecco's Modified Eagle Medium

FCS fetal calf serum FCS fetal calf serum

PBS phosphate-buffered saline

RLU relative luminescence units
ROS reactive oxygen species
ACP amorphous calcium phosphate
MCS metastable calcifying solution

References

World Health Organization. Fragility Fractures; WHO Fact Sheet. 2024. Available online: https://www.who.int/news-room/fact-sheets/detail/fragility-fractures (accessed on 2 October 2025).

- Svedbom, A.; Hernlund, E.; Ivergård, M.; Compston, J.; Cooper, C.; Stenmark, J.; McCloskey, E.V.; Jönsson, B.; Kanis, J.A. Epidemiology and Economic Burden of Osteoporosis in Europe: Fragility Fractures in the EU6 Countries. *Arch. Osteoporos.* 2013, 8, 136. [CrossRef]
- Kanis, J.A.; Cooper, C.; Rizzoli, R.; Reginster, J.-Y.; on behalf of the Scientific Advisory Board of the European Society for Clinical and Economic Aspects of Osteoporosis (ESCEO) and the Committees of Scientific Advisors and National Societies of the International Osteoporosis Foundation (IOF). European Guidance for the Diagnosis and Management of Osteoporosis in Postmenopausal Women. Osteoporos. Int. 2019, 30, 3–44. [CrossRef] [PubMed]
- 4. Webster, K.E.; Aznar, J.M.; Evans, J.T.; Whitehouse, M.R.; Prieto-Alhambra, D.; Blom, A.W. Trends and Variation in the Incidence of Hip Fracture in Europe: A Population-Based Cohort Study of 704,762 Hip Fractures between 2014 and 2024. *Lancet Reg. Health Eur.* 2025, 40, 100798. [CrossRef]
- 5. Mohammadi, H.; Eslami, H.; Fathi, M.H. Bioactive Calcium Phosphate Coatings for Bone Implant Applications: A Review. *Coatings* **2023**, *13*, 1091. [CrossRef]
- 6. Guo, L.; Zhang, Y.; Yang, L.; Tang, B. Advances in Multifunctional Bioactive Coatings for Metallic Bone Implants. *Materials* **2023**, 16, 183. [CrossRef]
- 7. Fiedler, J.; Hennig, D.; Keller, J.; Götz, W.; Schwabe, P.; Rupp, F. Copper Source Determines Chemistry and Topography of Implant Coatings to Optimally Couple Cellular Responses and Antibacterial Activity. *Bioact. Mater.* **2022**, *13*, 159–174. [CrossRef]
- 8. Aunon, M.; Vázquez, J.; Romero, C.; Holgado, M.; Ortega, F.G. Femtosecond Laser Modified Metal Surfaces Alter Biofilm Architecture and Reduce Bacterial Biofilm Formation. *Nanoscale Adv.* **2023**, *5*, 3843–3854. [CrossRef]
- 9. Šimek, M.; Ryl, J.; Veselý, J.; Mušálek, R.; Jelínek, M. Advanced Micro- & Nanostructuring for Enhanced Biocompatibility of Stainless Steel by Multi-Beam and Beam-Shaping Technology. *Appl. Surf. Sci.* **2025**, *653*, 159892. [CrossRef]
- 10. Matei, A.T.; Visan, A.I.; Negut, I. Laser-Fabricated Micro/Nanostructures: Mechanisms, Fabrication Techniques, and Applications. *Micromachines* **2025**, *16*, 573. [CrossRef]
- 11. Feng, J.; Wang, J.; Liu, H.; Sun, Y.; Fu, X.; Ji, S.; Liao, Y.; Tian, Y. A Review of an Investigation of the Ultrafast Laser Processing of Brittle and Hard Materials. *Materials* **2024**, *17*, 3657. [CrossRef]
- 12. Niu, S.; Wang, W.; Liu, P.; Zhang, Y.; Zhao, X.; Li, J.; Xiao, M.; Wang, Y.; Li, J.; Shao, X. Recent Advances in Applications of Ultrafast Lasers. *Photonics* **2024**, *11*, 857. [CrossRef]
- 13. Zhang, H.; Wang, Y.; Zhao, Y.; Zhou, H.; Zhang, Z. Surface Modification of Stainless Steel for Enhanced Antibacterial Activity. *ACS Omega* **2024**, *9*, 12345–12354. [CrossRef]
- 14. Dorozhkin, S.V. Calcium Orthophosphates (CaPO₄): Occurrence and Properties. *Materials* **2022**, *15*, 5230. [CrossRef]
- 15. Alhalawani, A.M.; Lin, Z.; Lee, T.C.; Stenzel, M.H. Advances in Calcium Phosphate–Based Coatings for Orthopedic and Dental Implants: Structure, Properties, and Biological Performance. *Materials* **2023**, *16*, 1947. [CrossRef]
- 16. Lutey, A.H.A.; Gemini, L.; Romoli, L.; Lazzini, G.; Fuso, F.; Faucon, M.; Kling, R. Towards Laser-Textured Antibacterial Surfaces. *Sci. Rep.* **2018**, *8*, 10112. [CrossRef]
- 17. Wu, Y.; Zhou, H.; Zeng, Y.; Xie, H.; Ma, D.; Wang, Z.; Liang, H. Recent Advances in Copper-Doped Titanium Implants. *Materials* **2022**, *15*, 2342. [CrossRef]
- 18. Wojcieszak, D.; Kaczmarek, D.; Antosiak, A.; Mazur, M.; Rybak, Z.; Rusak, A.; Osekowska, M.; Poniedziałek, A.; Gamian, A.; Szponar, B. Influence of Cu–Ti Thin Film Surface Properties on Antimicrobial Activity and Viability of Living Cells. *Mater. Sci. Eng. C* 2015, 56, 48–56. [CrossRef]
- 19. Oyane, A.; Nakamura, M.; Sakamaki, I.; Shimizu, Y.; Miyata, S.; Miyaji, H. Laser-Assisted Wet Coating of Calcium Phosphate for Surface-Functionalization of PEEK. *PLoS ONE* **2018**, *13*, e0206524. [CrossRef]
- 20. AISI. Steel Products Manual: Stainless Steels; American Iron and Steel Institute: Washington, DC, USA, 1980.
- 21. Daskalova, A.; Angelova, L. Design of Surfaces with Persistent Antimicrobial Properties on Stainless Steel Developed Using Femtosecond Laser Texturing for Application in "High Traffic" Objects. *Nanomaterials* **2023**, *13*, 2396. [CrossRef]
- 22. Dutour Sikirić, M.; Gergely, C.; Elkaim, R.; Wachtel, E.; Cuisinier, F.J.G.; Füredi-Milhofer, H. Biomimetic organic-inorganic nanocomposite coatings for titanium implants. *J. Biomed. Mater. Res. A* **2009**, *89*, 759–771. [CrossRef]

23. Milisav, A.M.; Mičetić, M.; Dubček, P.; Sotelo, L.; Cantallops-Vilà, C.; Erceg, I.; Fontanot, T.; Bojanić, K.; Fiket, Ž.; Ivanić, M.; et al. Effect of Ag and Cu Doping on the Properties of ZnO Magnetron Sputtered Thin Films for Biomedical Applications. *Appl. Surf. Sci.* 2025, 690, 162623. [CrossRef]

- 24. *ISO* 21702:2019; Measurement of Antiviral Activity on Plastics and Other Non-Porous Surfaces. International Organization for Standardization (ISO): Geneva, Switzerland, 2019.
- 25. *EN 10088-1:2014*; Stainless Steels—Part 1: List of Stainless Steels. European Committee for Standardization (CEN): Brussels, Belgium, 2014.
- 26. Sadauskas, M.; Trusovas, R.; Kvietkauskas, E.; Vrubliauskaitė, V.; Stankevičienė, I.; Jagminienė, A.; Murauskas, T.; Balkauskas, D.; Belosludtsev, A.; Ratautas, K. Advancing Nanoscale Copper Deposition through Ultrafast-Laser-Activated Surface Chemistry. *Nanomaterials* **2025**, *15*, 830. [CrossRef]
- 27. Dywel, P.; Szczesny, R.; Domanowski, P.; Skowronski, L. Structural and micromechanical properties of Nd:YAG laser marking stainless steel (AISI 304 and AISI 316). *Materials* **2020**, *13*, 2168. [CrossRef]
- 28. Dhaiveegan, P.; Elangovan, N.; Nishimura, T.; Rajendran, N. Corrosion behavior of 316L and 304 stainless steels exposed to industrial-marine-urban environment: Field study. *RSC Adv.* **2016**, *6*, 47314–47324. [CrossRef]
- 29. Murthy, P.S.; Venugopalan, V.; Arunya, D.D.; Dhara, S.; Pandiyan, R.; Tyagi, A. Antibiofilm activity of nano-sized CuO. In Proceedings of the International Conference on Nanoscience, Engineering and Technology (ICONSET 2011), Chennai, India, 28–30 November 2011; pp. 580–583. [CrossRef]
- 30. Aksoy Akgul, F.; Akgul, G.; Yildirim, N.; Unalan, H.E.; Turan, R. Influence of thermal annealing on microstructural, morphological, optical properties and surface electronic structure of copper oxide thin films. *Mater. Chem. Phys.* **2014**, *147*, 987–995. [CrossRef]
- 31. Pasteris, J.D.; Wopenka, B.; Valsami-Jones, E. Bone and Tooth Mineralization: Insights from Raman Spectroscopy. *Biochim. Biophys. Acta* **2008**, *1830*, 2899–2908. [CrossRef]
- 32. Furlani, M.; Notarstefano, V.; Riberti, N.; D'Amico, E.; Pierfelice, T.V.; Mangano, C.; Giorgini, E.; Iezzi, G.; Giuliani, A. Healing Kinetics of Sinus Lift Augmentation Using Biphasic Calcium Phosphate Granules: A Case Series in Humans. *Bioengineering* 2025, 12, 848. [CrossRef]
- 33. Hilton, J.; Nanao, Y.; Flokstra, M.; Askari, M.; Smith, T.K.; Di Falco, A.; King, P.D.C.; Wahl, P.; Adamson, C.S. The Role of Ion Dissolution in Metal and Metal Oxide Surface Inactivation of SARS-CoV-2. *Appl. Environ. Microbiol.* **2024**, *90*, e01553-23. [CrossRef]
- 34. Dorozhkin, S.V. Calcium Orthophosphates in Nature, Biology and Medicine. Materials 2009, 2, 399–498. [CrossRef]
- 35. Jiang, P.; Zhang, Y.; Hu, R.; Shi, B.; Zhang, L.; Huang, Q.; Yang, Y.; Tang, P.; Lin, C. Advanced Surface Engineering of Titanium Materials for Biomedical Applications: From Static Modification to Dynamic Responsive Regulation. *Bioact. Mater.* **2023**, 27, 15–57. [CrossRef]
- 36. Jahani, S.; Wang, L. The Effects of Surface Roughness on the Functionality of Ti13Nb13Zr Orthopedic Implants. *Materials* **2021**, 14, 3546. [CrossRef]
- 37. Rey, C.; Combes, C.; Drouet, C.; Glimcher, M.J. Bone mineral: Update on chemical composition and structure. *Osteoporos. Int.* **2007**, *20*, 1013–1021. [CrossRef]
- 38. Kokubo, T.; Takadama, H. How useful is SBF in predicting in vivo bone bioactivity? Biomaterials 2006, 27, 2907–2915. [CrossRef]
- 39. Liang, C.; Wang, H.; Yang, J.; Cai, Y.; Hu, X.; Yang, Y.; Li, B.; Li, H.; Li, H.; Li, C.; et al. Femtosecond Laser-Induced Micropattern and Ca/P Deposition on Ti Implant Surface and Its Acceleration on Early Osseointegration. *ACS Appl. Mater. Interfaces* **2013**, *5*, 8179–8186. [CrossRef]
- 40. Wu, X.; Ao, H.; He, Z.; Wang, Q.; Peng, Z. Surface Modification of Titanium by Femtosecond Laser in Reducing Bacterial Colonization. *Coatings* **2022**, *12*, 414. [CrossRef]
- 41. Su, W.; Zhang, M.; Liu, L.; Xu, R.; Huang, Z.; Shi, Z.; Liu, J.; Li, Z.; Li, X.; Hao, P.; et al. Femtosecond Laser Treatment Promotes the Surface Bioactivity and Bone Ingrowth of Ti6Al4V Bone Scaffolds. *Front. Bioeng. Biotechnol.* **2022**, *10*, 962483. [CrossRef]
- 42. Meister, T.L.; Fortmann, J.; Breisch, M.; Sengstock, C.; Steinmann, E.; Köller, M.; Pfaender, S.; Ludwig, A. Nanoscale Copper and Silver Thin Film Systems Display Differences in Antiviral and Antibacterial Properties. *Sci. Rep.* **2022**, *12*, 7193. [CrossRef] [PubMed]
- 43. Rakowska, P.D.; Tiddia, M.; Faruqui, N.; Bankier, C.; Pei, Y.; Pollard, A.J.; Zhang, J.; Gilmore, I.S. Antiviral Surfaces and Coatings and Their Mechanisms of Action. *Commun. Mater.* **2021**, 2, 53. [CrossRef]

Disclaimer/Publisher's Note: The statements, opinions and data contained in all publications are solely those of the individual author(s) and contributor(s) and not of MDPI and/or the editor(s). MDPI and/or the editor(s) disclaim responsibility for any injury to people or property resulting from any ideas, methods, instructions or products referred to in the content.